

Numerical simulation of corona in electrical equipment operated at high altitude

Yue Zhang(张跃), Zhou Huang(黄洲), Xue-Ming Shen(沈雪明), Gen-Bo Zhang(张根博), and Wen-Jun Ning(宁文军)

Citation: Chin. Phys. B, 2026, 35 (**7**): 075202. DOI: 10.1088/1674-1056/ae1565
http://cpb.iphy.ac.cn; http://iopscience.iop.org/cpb

What follows is a list of articles you may be interested in

Numerical investigation on performance of electrohydrodynamic thruster with needle-ring electrode

Chun-Yan Wang(王春岩), Hu-Lin Huang(黄护林), Hao Li(李灏), Tian-Tian Chen(陈田田), and Xi-Jing Hu(胡锡精)
Chin. Phys. B, 2026, 35 (**3**): 035205. DOI: 10.1088/1674-1056/adf829

Experimental and numerical analyses of electrohydrodynamic force according to air pressure

Rong-Hui Quan(全荣辉), Bo Wang(王博), and Yun-Jia Yao(姚韵佳)
Chin. Phys. B, 2023, 32 (**6**): 065201. DOI: 10.1088/1674-1056/acac11

Fractal microstructure of Ag film via plasma discharge as SERS substrates

Xue-Fen Kan(阚雪芬), Cheng Yin(殷澄), Zhuang-Qi Cao(曹庄琪), Wei Su(苏巍), Ming-Lei Shan(单鸣雷), and Xian-Ping Wang(王贤平)
Chin. Phys. B, 2021, 30 (**12**): 125201. DOI: 10.1088/1674-1056/ac0693

Review on ionization and quenching mechanisms of Trichel pulse

Anbang Sun(孙安邦), Xing Zhang(张幸), Yulin Guo(郭雨林), Yanliang He(何彦良), and Guanjun Zhang(张冠军)
Chin. Phys. B, 2021, 30 (**5**): 055207. DOI: 10.1088/1674-1056/abd75d

Enhancement of corona discharge induced wind generation with carbon nanotube and titanium dioxide decoration

Jianchun Ye(叶建春), Jun Li(李俊), Xiaohong Chen(陈晓红), Sumei Huang(黄素梅), Wei Ou-Yang(欧阳威)
Chin. Phys. B, 2019, 28 (**9**): 095202. DOI: 10.1088/1674-1056/ab33ed

---

Numerical simulation of corona in electrical equipment operated at high altitude

Yue Zhang(张跃)[1,2], Zhou Huang(黄洲)[1], Xue-Ming Shen(沈雪明)[3], Gen-Bo Zhang(张根博)[2], and Wen-Jun Ning(宁文军)[3,†]

[1] *State Key Laboratory of Electrical Insulation and Power Equipment, School of Electrical Engineering, Xi'an Jiaotong University, Xi'an* 710049, *China*
[2] *Dongfang Electric Machinery Co., Ltd., Deyang* 618000, *China*
[3] *College of Electrical Engineering, Sichuan University, Chengdu* 610065, *China*

(Received 22 June 2025; revised manuscript received 15 September 2025; accepted manuscript online 21 October 2025)

Corona discharge is a common form of electrical fault in power equipment. Studying corona at different altitudes is essential for ensuring reliable operation of electrical systems under varying environmental conditions. In this work, a Multiphysics simulation model of corona discharge was developed to investigate the discharge behavior and induced ionic wind characteristics under different air pressures. First, the accuracy of the simulation model was validated by experiments. At 1 bar (1 bar = 10^5 Pa), Trichel pulses with an amplitude of 1.1 mA and a repetition frequency of 250 kHz were observed, along with a maximum ionic wind velocity of 9.49 m/s in the discharge channel. When the pressure was reduced to 0.79 bar, the discharge was overall enhanced, with the Trichel pulse amplitude decreasing to 0.5 mA, the repetition frequency increasing to 760 kHz, and the induced ionic wind becoming stronger. Both the velocity within the channel and the gap increased with decreasing pressure. This study provided a theoretical reference for the deployment and operation of electrical equipment in high-altitude environments.

Keywords: corona discharge, plasma simulation, plasma dynamics and flow

PACS: 52.80.Hc, 52.65.–y, 52.30.–q

DOI: 10.1088/1674-1056/ae1565 **CSTR:** 32038.14.CPB.ae1565

1. Introduction

With the continuous construction of DC transmission projects in China, more electrical equipment will be deployed in high-altitude areas. Due to the climate characteristics of low air density and low air pressure in high-altitude areas, the operating reliability of electrical equipment in such an environment is currently the focus of academic attention. Corona discharge is a common form of local discharge in electrical equipment.[1] The electrical corrosion and chemical corrosion of the discharge will damage the insulation performance of the equipment, and under certain conditions, they will cause violent discharges such as sparks or arcs. Therefore, it is generally believed that corona discharge is a precursor to insulation failure of electrical equipment.[2] Therefore, it is necessary to study the characteristics of corona discharge in high-altitude environments to provide theoretical guidance for how to diagnose corona discharge in the early stage of discharge development (*i.e.*, low discharge current) and propose corresponding suppression measures.

The study of corona discharge characteristics began in the 1930s.[3] Scholars combined experiments and simulations to conduct a preliminary diagnosis of the characteristics of corona discharge.[4–6] The results show that there is a characteristic pulse current (Trichel pulse) in negative polarity corona discharge, which has the characteristics of strong periodicity and a steep rising edge, and is one of the characteristics of negative polarity corona. Subsequently, scholars conducted a series of studies on the characteristics of the Trichel pulses.[7–11]

Zhang *et al.*[7] used ICCD to photograph the time variation of Trichel pulses and measured the luminescence spectra of N_2 molecules and N_2^+ using a spectrometer. Meng *et al.*[8] constructed an ultrafast optical counting and performance system to measure the luminescence characteristics of Trichel pulses in time and space based on an extremely high time resolution of 55 ps. Li *et al.*[9,10] experimentally measured the current characteristics of Trichel pulses in longer gaps (10.5 cm–50 cm) and shorter gaps (4 cm–5.5 cm) under different applied voltages.

With the in-depth study of the characteristics of corona discharge, scholars found that a directional airflow is generated inside the gap during discharge, because when discharge occurs, charged particles transfer energy through continuous movement and mutual collisions.[12,13] When some ions collide with neutral molecules, they transfer kinetic energy, thereby driving the movement of neutral molecules. This process is called corona discharge-induced ionic wind. In view of the characteristics of ionic wind, Moreau *et al.*[14–16] conducted a series of studies and summarized the calculation formula for the ionic wind propulsion force. They also took im-

[†]Corresponding author. E-mail: ningwj@scu.edu.cn

© 2026 Chinese Physical Society and IOP Publishing Ltd. All rights, including for text and data mining, AI training, and similar technologies, are reserved.

ages of the flow field of the ionic wind using the PIV system and systematically summarized the characteristics of corona-induced ionic wind. In addition, some scholars have studied the characteristics of ionic wind generated by different electrode shapes.[17,18]

With the development of experimental technology, people have a preliminary understanding of the formation mechanism and macroscopic characteristics of corona discharge. However, since corona discharge is a fast, weak luminous discharge, it is difficult to analyze its microscopic characteristics by experiments alone. Therefore, while developing experimental technology, scholars are also exploring corona discharge simulation technology.

Morrow[6] first established a one-dimensional (1D) simulation model of corona discharge in 1985. On this basis, scholars expanded the simulation fluid model from one dimension to two dimensions[19,20] and continuously optimized the calculation method of the model.[21,22] Subsequently, Kang *et al.*[23] proposed a simplified set of simulation parameters based on the experimental results of Kulikovsky.[24] Tran *et al.*[25] applied the parameters to simulate the discharge process of negative corona, successfully simulated a series of flow pulse waveforms, and intuitively demonstrated the distribution state of charged particles in a single pulse. Dordizadeh *et al.*[26–28] followed this model and conducted a detailed analysis of the pulse development process. Based on the above model, Chen *et al.*[29,30] established a model that couples the thermal field and the flow field, so that the model could be applied to the calculation of ionic wind.

At present, scholars have combined experiments and simulations to deeply explore the dynamic behavior and generation mechanism of corona discharge,[25,29,31–34] and have achieved certain results. However, there are still certain limitations in adapting to complex discharge conditions and multi-physical field coupling characteristics. In the present study, we extended the atmospheric-pressure negative corona model[28,35] to high altitude scenarios by adjusting the input parameters according to the gas pressure and temperature. Besides, ionic wind and the thermal effect induced by the Trichel pulses were studied, aiming to present a more comprehensive understanding of the multi-physics of Trichel pulses under various conditions. The rest of the paper is organized as follows. In Section 2, a description of the numerical model and experimental setup is given as the first part, followed by the model validation via comparisons between model predictions and experiments. Section 3 presents the typical results on Trichel pulses and the parametric studies. In Section 4, a brief discussion of the results is given. Conclusions are summarized in Section 5.

2. Modeling and experiments

2.1. Model introduction

This paper uses the classical three-particle hydrodynamic model to describe the discharge dynamics of the negative corona. The motion of electrons, positive ions, and negative ions is described by combining three continuity equations:

$$\begin{aligned}&\frac{\partial n_\mathrm{e}}{\partial t}+\nabla(-\mu_\mathrm{e}\boldsymbol{E}n_\mathrm{e}-D_\mathrm{e}\nabla n_\mathrm{e})\\&=\alpha n_\mathrm{e}|\mu_\mathrm{e}\boldsymbol{E}|-\eta n_\mathrm{e}|\mu_\mathrm{e}\boldsymbol{E}|-k_\mathrm{ep}n_\mathrm{e}n_\mathrm{p},\end{aligned}\tag{1}$$

$$\frac{\partial n_\mathrm{p}}{\partial t}+\nabla\cdot(\mu_\mathrm{p}\boldsymbol{E}n_\mathrm{p}-D_\mathrm{p}\nabla n_\mathrm{p})=\alpha n_\mathrm{e}|\mu_\mathrm{e}\boldsymbol{E}|-k_\mathrm{ep}n_\mathrm{e}n_\mathrm{p},\tag{2}$$

$$\frac{\partial n_\mathrm{n}}{\partial t}+\nabla\cdot(-\mu_\mathrm{n}\boldsymbol{E}n_\mathrm{n}-D_\mathrm{n}\nabla n_\mathrm{n})=\eta n_\mathrm{e}|\mu_\mathrm{e}\boldsymbol{E}|-k_\mathrm{np}n_\mathrm{n}n_\mathrm{p}.\tag{3}$$

The right-hand side terms of Eqs. (1)–(3) represent the collision processes considered in the model, including: impact ionization (ionization coefficient α), attachment of electrons to neutral molecules (attachment coefficient η), recombination reaction of electrons to positive ions (recombination reaction coefficient k_ep), and recombination reaction of positive ions to negative ions (reaction coefficient k_np). The electric field vector $\boldsymbol{E}$ (including both the Laplacian electric field and space-charge-built one) is calculated using Poisson's equation

$$\nabla\cdot\boldsymbol{E}=\frac{e(n_\mathrm{p}-n_\mathrm{e}-n_\mathrm{n})}{\varepsilon_0}.\tag{4}$$

The ionic wind and thermal effects caused by corona discharge are calculated by the Navier–Stokes equation (5) and the heat conduction equation (7), where F_ehd is the ionic wind propulsion force, P_heat is the heat source, C_p is the specific heat capacity of the gas at constant pressure, j is the current density, q_g is the gas density, and ξ_ex is the proportion of electric power used for heating in the gas. Equations (6) and (8) are used to calculate the ionic wind propulsion force F_ehd and the heat source P_heat, respectively,

$$\rho_\mathrm{g}\left(\frac{\partial\boldsymbol{u}}{\partial t}+\boldsymbol{u}\cdot\nabla\boldsymbol{u}\right)=-\nabla p+\mu_\mathrm{v}\nabla^2\boldsymbol{u}+F_\mathrm{ehd},\tag{5}$$

$$F_\mathrm{ehd}=e(n_\mathrm{p}-n_\mathrm{e}-n_\mathrm{n})\boldsymbol{E},\tag{6}$$

$$\rho_\mathrm{g}C_\mathrm{p}\frac{\partial T}{\partial t}+\rho_\mathrm{g}C_\mathrm{p}\boldsymbol{u}\cdot\nabla T-\nabla\cdot(k_\mathrm{T}\nabla T)=P_\mathrm{heat},\tag{7}$$

$$P_\mathrm{heat}=(\boldsymbol{j}_\mathrm{p}-\boldsymbol{j}_\mathrm{n})\cdot\boldsymbol{E}-\xi_\mathrm{ex}\boldsymbol{j}_\mathrm{e}\cdot\boldsymbol{E}.\tag{8}$$

Previous research showed[19] that secondary electron emission is an important mechanism for maintaining negative charge. In this model, the secondary electron emission induced by positive ions impacting the cathode surface is calculated by

$$\Gamma_\mathrm{e}=\gamma n_\mathrm{p}u_\mathrm{p}\,|\boldsymbol{E}|\,,\tag{9}$$

where Γ_e is the surface secondary electron flux, γ is the secondary electron emission coefficient, and its value is 0.01 in the simulation.[27,35] The parameter settings of the model are shown in Table 1.

Table 1. Simulation parameters.[22,25,27]

Parameter	Value	Unit
Ionization coefficient	$1.4\times10^{-20}\times N\times\exp(-6.6\times10^{-19}/E_{\rm N})$	1/m
Attachment coefficient	$6.23\times10^{-23}\times N\times\exp(-1\times10^{-19}/E_{\rm N})$	1/m
Coefficient of recombination of positive and negative ions	2×10^{-13}	m^3/s
Coefficient of recombination of positive ions and electrons	2×10^{-13}	m^3/s
Mobility of electrons	$1.92\times(2.5\times10^{25}\times E_{\rm N})^{-0.25}$	$m^2/(V\cdot s)$
Mobility of positive ions	$2.43\times10^{-4}(P_0/P_x)$	$m^2/(V\cdot s)$
Mobility of negative ions	$2.7\times10^{-4}(P_0/P_x)$	$m^2/(V\cdot s)$
Diffusion coefficient of electrons	0.18	m^2/s
Diffusion coefficient of positive ions	$2.8\times10^{-6}(T_x/T_0)$	m^2/s
Diffusion coefficient of negative ions	$4.3\times10^{-6}(T_x/T_0)$	m^2/s

Note: N is the total number density in unit m^{-3}; $E_{\rm N}$ is the reduced electric field in units $V\cdot m^2$; $P_0=1$ atm (1 atm = 1.01325×10^5 Pa), $T_0=300$ K while P_x and T_x are gas pressure and temperature at specified conditions, respectively.

The input parameters are adopted from literatures with gas pressure of 1 atm, and therefore scaling should be done for varying gas pressure (caused by the change of altitude). Please note the fact that gas discharges are determined by the reduced parameters rather than their practical value, *i.e.*, the ionization or attachment coefficient are functions on the reduced electric field $E_{\rm N}$ ($E_{\rm N}=E/N$), but not solely depend on E. As such, the mobility and diffusion coefficients are scaled with the first order of total particle number density N (or pressure P or temperature T determined by the idea gas law $N=k_{\rm B}T/P$), as indicated in Table 1.

Geometry and mesh grid of the simulation domain is shown in Fig. 1. In a two-dimensional (2D) symmetric geometry, the simulation domain is set as 30 mm×20 mm in r and z directions, respectively. Although the discharge plasma is mostly confined around the needle tip the axis of symmetry, the much larger simulation domain guarantees a more realistic boundary condition of the open boundaries (see Fig. 1) when calculating the electric field and the thermal-flow fields. The metal needle electrode is connected to a negative DC source, while the plate electrode is grounded. The needle electrode is composed of a hyperbola with a curvature radius of 250 μm and an air gap of 10 mm. In the vicinity of the needle tip, fine mesh of 4 μm is set to numerically resolve the steep gradient of the corona discharge. The mesh size gradually increased to 80 μm in the rest of the gas–gap region (z direction), where the plasma was likely to migrate to with moderately high density. While in the r direction, the mesh size is much coarser but proved to be fine enough to capture the gradient of thermal-flow fields. The total number of mesh grids is about 4.2×10^5. Validation of the mesh size independence is done before discussion. By setting the finest size to 1 μm at the needle tip and a total mesh grid of about 8×10^5 of the simulation domains, the physics and quantities of the corona discharge, the flow field and the thermal field are technically identical, but with three times higher of calculation time.

In the simulation, it is assumed that the initial density of electrons and positive ions followed a Gaussian distribution with a peak value $n_{\rm max}=10^{16}$ (in units of m^{-3})

$$n_{\rm e}=n_{\rm p}=n_{\rm max}\left(-\frac{(r-r_0)^2}{2s_0^2}-\frac{(z-z_0)^2}{2s_0^2}\right). \tag{10}$$

The corona current can be calculated by Sato's formula

$$i=\frac{1}{|V|}\int_{\Omega}\boldsymbol{E}\cdot\boldsymbol{E}_{\rm L}\cdot\sum_{\rm e,p,n}n_{\rm j}\mu_{\rm j}\,{\rm d}\Omega, \tag{11}$$

where $\boldsymbol{E}_{\rm L}$ is the Laplace electric field.

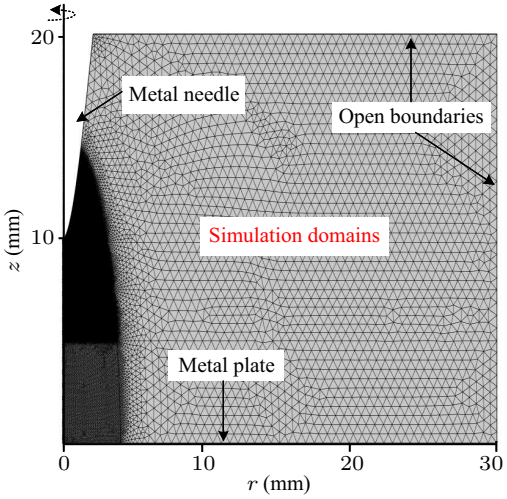


Fig. 1. Geometry and mesh grid of the simulation domain.

2.2. Experiment setup

Figure 2 shows the main experimental setup. The needle electrode used for discharge was a gold-plated probe with a length of 50 mm and a radius of curvature of 250 μm, and the plate electrode was a brass plate with a radius of 50 mm. The distance between the two electrodes was 10 mm as in the simulation. The needle electrode was connected to a high-voltage power supply. The power supply used in the experiment was a power supply that could generate a negative DC voltage of 0 kV∼ −30 kV (Dongwen DWN3031ACD1). In the present study, the applied voltage was set as −7 kV. The plate electrode was grounded via a 200-Ω non-inductive resistor in series. The resistor was used to measure the current in the circuit

by a parallel voltage probe that was connected to an oscilloscope (Tektronix MDO3104). It should be mentioned that the voltage probe was connected in the direction of current flow, and therefore the measured voltage (or the current) waveform was positive.

In addition, a development device is built using a smoke generator, an acrylic sealed box, a laser (MGL-V-532), and a high-speed camera (MEMRECAM ACS-4 M16) to display the changes in the flow field during the discharge process. Before the experiment began, the prism direction was adjusted to distribute the laser throughout the discharge gap, the frame rate of the high-speed camera was adjusted to 1000 fps, and the shooting time was 30 s. Subsequently, the smoke filled the entire acrylic sealed box and the box was quickly sealed. After there was no obvious difference in light and dark in the sealed box, the high-voltage power supply and the high-speed camera were started to capture the flow field morphology of the ionic wind during the discharge process. Figures 2(b) and 2(c) show the distribution of the laser irradiation cross section and the background smoke field during the experiment.

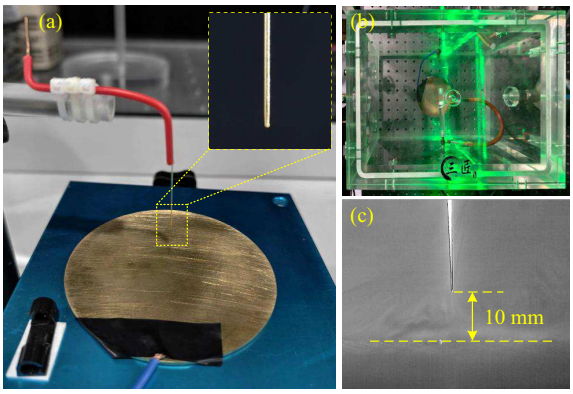


Fig. 2. Experiment setup: (a) needle-plate electrode configuration, (b) laser irradiation cross section for flow field virtualization, and (c) background smoke field.

2.3. Model validation

To ensure the validity of the model, the simulation results obtained under the same conditions are first compared with the experimental results. The comparisons of Trichel pulse waveforms are shown in Fig. 3.

The Trichel pulse amplitude obtained by the experiment is about 1.1 mA and the frequency is 250 kHz. The pulse amplitude calculated by simulation is 1.1 mA and the frequency is 300 kHz. The current waveform matches well.

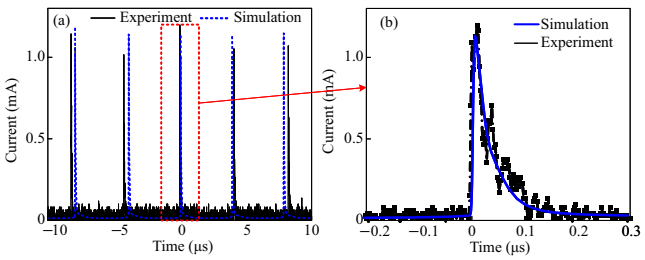


Fig. 3. Comparisons of Trichel pulses from experiments and simulations: (a) pulse sequences and (b) a single pulse.

The flow field distribution morphology obtained by experiment and simulation is compared as shown in Fig. 4. The main channels of the ionic wind are located directly below the needle electrode, and the flow field streamlines on both sides are the same. The simulation results of the ionic wind also have a high degree of matching with the experiment. It can be considered that the model as a whole provides a certain reference.

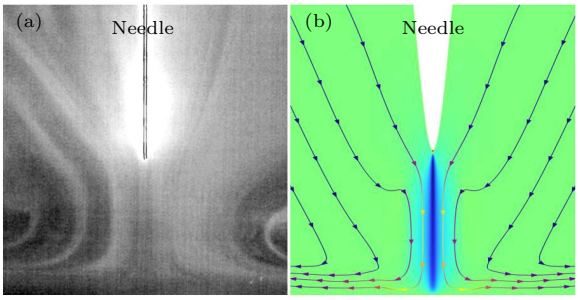


Fig. 4. Comparisons of the ionic-wind-induced flow field distributions between (a) experiment and (b) simulation.

3. Results

3.1. Trichel pulse and ionic wind characteristics under atmospheric pressure

The simulation results obtained at an applied voltage level of −7 kV and a gas pressure of 1 bar are selected as the basic case. The Trichel current waveform obtained under the above conditions is shown in Fig. 5, with a pulse amplitude of approximately 1.1 mA and a repetition frequency of 300 kHz.

The simulation results in Fig. 5 are used as input items to calculate the flow field distribution of the ionic wind induced by the corona and the gas temperature distribution in the gap after the current heats the gas. Figure 6(a) shows the flow field distribution of the ionic wind. The arrows in the figure indicate the direction of the airflow.

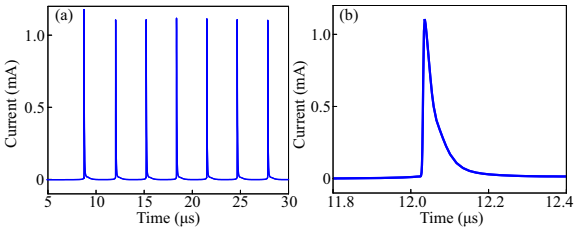


Fig. 5. Trichel pulse current obtained by simulation: (a) pulse sequence and (b) single pulse.

The flow field distribution obtained by simulation calculation is consistent with the smoke development result. The main airflow channel is located directly below the needle electrode. The flow velocity in the channel can reach up to 6.89 m/s, and the direction points to the plate electrode. However, the simulation results show that within the range of 25 μm (corresponding to the ionization zone) near the tip electrode, there is a high-speed area with the airflow direction pointing to the tip of the electrode. The maximum flow velocity in this area can reach 9.49 m/s.

Since the ionic wind originates from the momentum transfer between ions and neutral molecules, its airflow direction and flow velocity are related to the polarity of the ions.[12] The airflow direction in the high-speed area near the needle electrode is consistent with the movement direction of the positive ions in the ionization zone, and is mainly dominated by the positive ions moving toward the needle electrode, forming an ionic wind pointing to the needle electrode. The migration zone in the gap is dominated by negative ions moving toward the plate electrode, so an ionic wind pointing to the plate electrode is generated. Due to the multiple negative ion clouds in the gap, the neutral molecules in the gap are continuously accelerated, and the airflow channel continues to extend downward to the vicinity of the plate electrode.

The main airflow channel is located on the symmetry axis, and the flow velocity on the axis can reflect the flow characteristics of the ionic wind in the discharge gap. The velocity distribution on the axis is plotted in Fig. 6(c). The line graph shows a high velocity region in the ionization zone, with the flow direction pointing toward the tip electrode. The velocity then decreases rapidly and reverses in the drift region, where the gas velocity decreases with increasing axial distance and eventually drops rapidly to zero at the plate electrode.

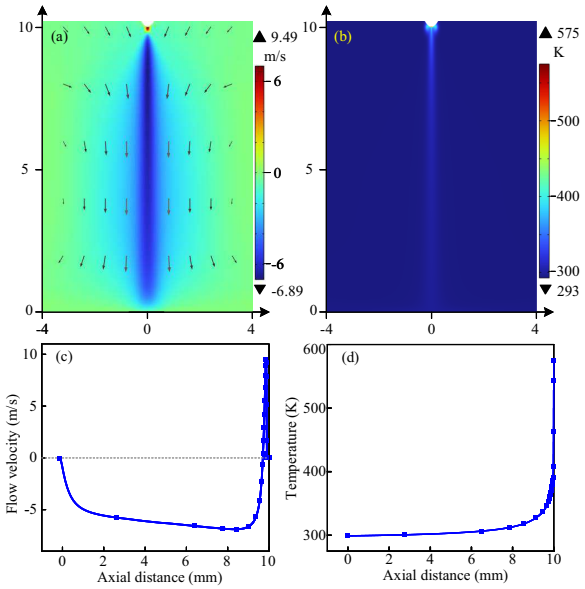


Fig. 6. Characteristics of the Trichel pulse current obtained by simulation: (a) ionic wind, (b) thermal, flow velocity (c), and temperature (d) along the symmetric axis.

Figures 6(b) and 6(d) show the temperature rise trend of the gas caused by the thermal effect of the corona current in the gap. Since the corona current generated by the needle-plate structure is relatively weak (the average value is tens of microamperes), the temperature rise caused by heating the gas through the thermal effect of the current is limited. The high-temperature area is mainly concentrated near the tip of the needle, with the highest temperature reaching 575 K, which decays rapidly outside the ionization zone, and the average temperature on the symmetry axis is about 302 K. From a microscopic perspective, when charged particles collide with neutral molecules, they transfer kinetic energy to the molecules, resulting in intensified molecular thermal motion, which is manifested as a temperature rise of the gas at a macroscopic level. In the ionization zone, frequent collisions produce a significant temperature rise, and then the heat is transferred outward by convection, diffusion, *etc*. Due to the guidance of the ionic wind on the airflow, the heat mainly diffuses downward along the symmetry axis.

3.2. Trichel pulse characteristics under different gas pressures

In order to explore the discharge characteristics at high altitude, the air pressure in the air gap is reduced to 0.78 bar (1 bar = 10^5 Pa), corresponding to an altitude of 2000 m. The amplitude-frequency characteristics of Trichel pulses and the time-averaged current change trend of corona under different air pressures are shown in Fig. 7.

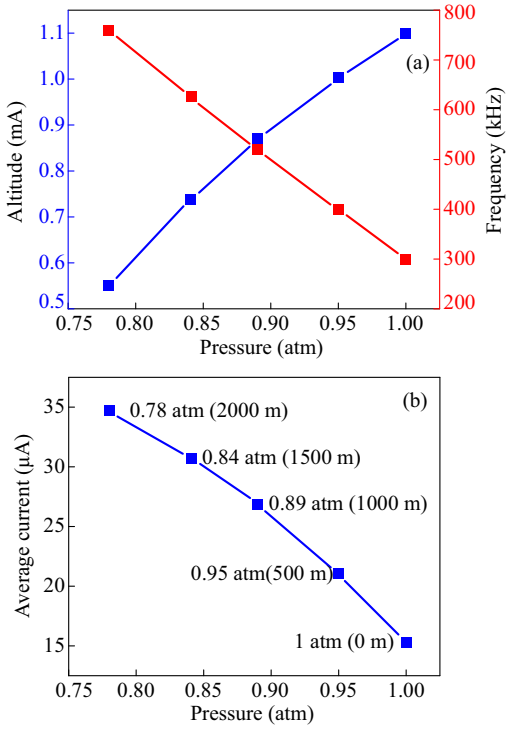


Fig. 7. Trichel pulses at different gas pressure: (a) the peak value and the repeating frequency, (b) time-averaged current, 5 pressure points are shown with the value in units of atm and corresponding altitude value in units of m.

When the air pressure dropped from 1 bar to 0.78 bar, the pulse amplitude dropped from 1.1 mA to 0.5 mA, and the pulse repetition frequency increased from 300 kHz to 760 kHz. The time-averaged current increased from 15 μA to 34 μA. The change trend of the total number of three charged particles under different air pressures is shown in Fig. 8. At low air pressure, the total number of positive ions and electrons was less, and negative ions accounted for a larger proportion of the total number of charged particles.

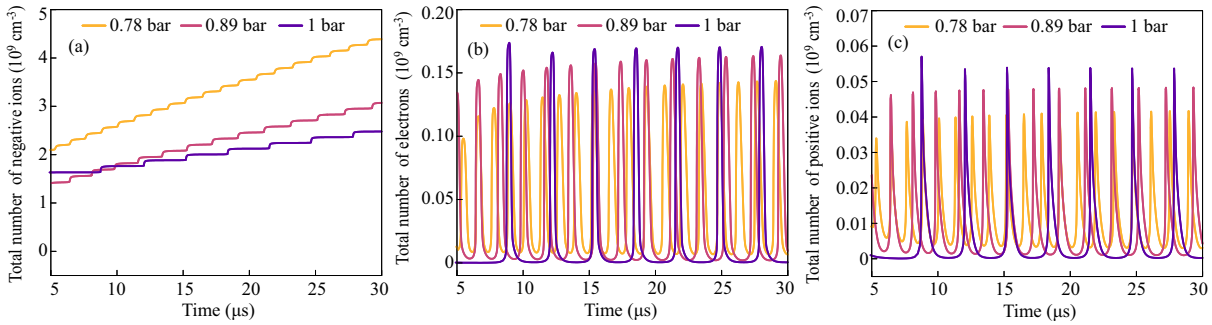


Fig. 8. Trend of charged particles under different pressures: (a) negative ions, (b) electrons, and (c) positive ions.

3.3. Characteristics of ionic wind under different air pressures

Subsequently, the effect of air pressure on the thermal field and ionic wind flow field characteristics is further calculated. When the air pressure is 1 bar (pressure at sea level), 0.89 bar (pressure at 1000-m altitude) and 0.78 bar (pressure at 2000-m altitude), the trends of the gas temperature and gas flow rate on the symmetry axis are shown in Fig. 9.

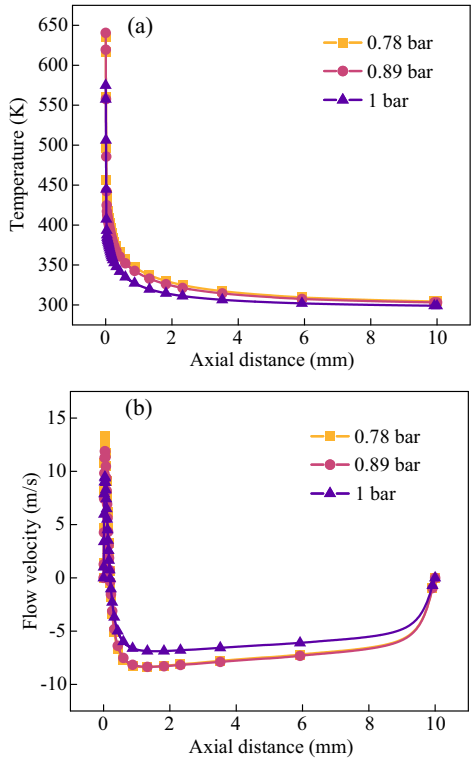


Fig. 9. Distribution of (a) gas temperature and (b) gas velocity on the symmetry axis under different pressures.

Among them, as the air pressure decreases, the temperature rise in the gap becomes more obvious. When the air pressure dropped from 1 bar to 0.78 bar, the maximum gas temperature in the gap increased from 574 K to 635 K. The gas flow rate in the channel also increased from 6.89 m/s to 8.37 m/s. The maximum flow rate in the ionization zone increased from 9.49 m/s to 13.38 m/s. Figure 10 shows the change trend of the maximum gas flow rate in the gap and the main channel of the ionic wind. Overall, with the increase of air pressure, the maximum flow rate in the channel and the gap decrease.

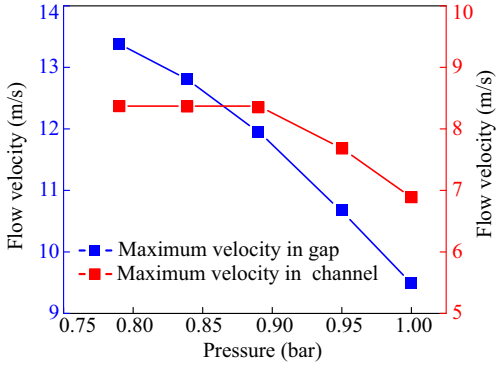


Fig. 10. Maximum flow velocity in gap and in the ionic wind channel under different pressures.

4. Discussion

According to the theory of Trichel pulses,[6,29,34,35] the transport of the negative ion cloud determines the periodic formation and extinguishing of the pulses. That is to say, after the first breakdown, positive ions are concentrated around the needle tip, while the negative ions drift towards the grounded plate electrode (anode), as illustrated in Fig. 11. Electrons do not contribute at this stage because of the very high mobility and the fast dissipation into the anode. Separation of the positive and negative ions leads to the formation of space charge, which will build an electric field E_s that is opposite to the applied one (the Laplacian electric field E_L), and thus weakens the whole electric field strength and eventually quenches the pulse. As the negative ion cloud continues to move away from the needle electrode, the counterpart electric field strength is reduced, meaning the electric field at the needle tip E_{tip} recovers. Another discharge pulse will emerge once E_{tip} reaches a certain value.[21,29] Repeating the process results in the formation of Trichel pulses.

By reducing the air pressure, the gas density N decreases, while the critical value of E/N for corona inception remains almost unchanged for the gas pressure range considered in the present work.[36] As such, the corona discharge will emerge at a lower E value at lower pressure. Since E_{tip} is equal to $E_L - E_{sx}$ as shown in Fig. 11, E_{sx} will be higher than E_s at

the discharge inception moment, implying that the drift length l_{dx} of the negative ions is shorter for the lower pressure cases. Meanwhile, the ion drift velocity V_d equals $E \times \mu_i = (E/N) \times (\mu_i N) = (E/N) \times \mu_{0N}$, where μ_i is the pressure-dependent ion mobility, μ_{0N} is the reduced ion mobility at atmospheric pressure. Thus, the drift velocity of the negative ion cloud remains the same for different gas pressures. Therefore, it requires less time for the negative ion to move to the position where the next discharge event can emerge. In other words, the repeating frequency of the Trichel pulse increases at lower gas pressure, as shown in Figs. 7(a) and 8.

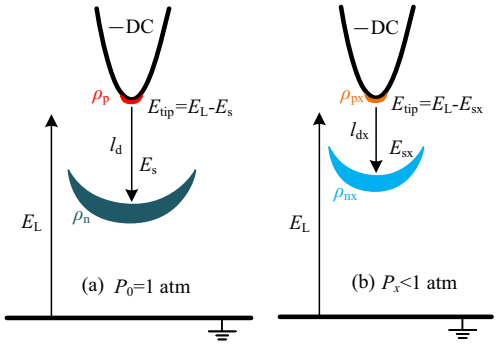


Fig. 11. Schematic diagram of formation of Trichel pulses: (a) at atmospheric pressure, (b) at lower pressure. Distribution and parameters in the figure are for the moment right before the inception of an Trichel pulse.

The ionization coefficient α is proportional to N (see Table 1) at the inception inception condition where the reduced electric field kept almost the same respect to the change of gas pressure.[36] That is to say, the Trichel pulses are emerged with lower initial α under lower pressure. Please note the current density $J \approx e\Gamma_e \approx n_e V_d \propto n_e \propto \exp(\alpha d)$, where d is the characteristic ionization length of the corona discharge, it is expected the current peak of Trichel pulse at lower pressure is lower, as predicted by the model and shown in Fig. 7(a). However, the time-averaged current shows an increased trend with reducing air pressure (Fig. 7(b)), which should be attributed to the higher increasing rate of the repeating frequency that surpassed the declining rate of the peak value.

The above-mentioned mechanism is also applied to explain the phenomenon that the time-averaged ion density increases at lower pressure. Since the ionic wind originates from the momentum transfer between ions and neutral molecules, the induced ionic wind speed increases with an increase in discharge. At the same time, more intense discharge also enhances the thermal effect caused by it, so the maximum temperature in the gap increases.

5. Conclusion

This paper used a multi-physics simulation model to study the negative polarity corona discharge at high altitude and the characteristics of the ionic wind induced by it. It is clear that the microscopic characteristics of the discharge and ionic wind under different air pressures help to deepen the understanding of the microscopic morphology of corona discharge and the dynamic characteristics of the ionic wind induced by it. The specific conclusions are as follows:

(i) Under an external voltage of −7 kV and a discharge gap of 10 mm, Trichel pulses with an average amplitude of 1.1 mA and a repetition frequency of 300 kHz are generated. The discharge-induced ionic wind channel is mainly located below the needle electrode, and the maximum wind speed in the channel is 6.89 m/s.

(ii) As the ambient air pressure decreases from 1 bar to 0.78 bar, the discharge shows an overall strengthening trend. The pulse amplitude decreases from 1.1 mA to 0.5 mA, while the pulse repetition frequency increases from 250 kHz to 760 kHz. The time-averaged current increases from 15 μA to 34 μA.

(iii) As the air pressure decreases, the corona-induced ionic wind also increases, and the gas flow rate in the channel increases from 6.89 m/s to 8.37 m/s.

Acknowledgements

Project supported by DEC-SCU Joint Innovation Research Institute Project (Grant No. 24H1283) and the Key Research and Development Program of Xizang Autonomous Region (Grant No. XZ202403ZY0036).

References

[1] Černák M, Hoder T and Bonaventura Z 2020 *Plasma Sources Science and Technology* **29** 013001
[2] Hedtke S, Xu P, Pfeiffer M, Zhang B, He J and Franck C M 2019 *IEEE Transactions on Power Delivery* **35** 1038
[3] Trichel G W 1938 *Phys. Rev.* **54** 1078
[4] Lama W L and Gallo C F 1974 *J. Appl. Phys.* **45** 103
[5] Loeb L, Kip A, Hudson G and Bennett W 1941 *Phys. Rev.* **60** 714
[6] Morrow R 1985 *Phys. Rev. A* **32** 1799
[7] Zhang Y, Qin Y, Zhao G and Ouyang J 2016 *J. Phys. D: Appl. Phys.* **49** 245206
[8] Meng X, Song H, Sheng G and Jiang X 2023 *High Voltage* **8** 538
[9] Li Z, Zhang B, He J and Xu Y 2014 *Phys. Plasmas* **21** 012113
[10] Li Z, Zhang B and He J 2013 *Phys. Plasmas* **20** 093507
[11] Dong X G, Li B J and Li Y J 2024 *Chin. Phys. B* **33** 085203
[12] Quan R, Wang B and Yao Y 2023 *Chin. Phys. B* **32** 065201
[13] Zheng B, Liu Y, Yu M, Jin Y, Zhang Q and Chen Q 2023 *Chin. Phys. B* **32** 095203
[14] Moreau E, Sosa R and Artana G 2008 *J. Phys. D: Appl. Phys.* **41** 115204
[15] Moreau E, Audier P and Benard N 2018 *Journal of Electrostatics* **93** 85
[16] Moreau E and Benard N 2024 *Journal of Electrostatics* **132** 103988
[17] Grosse S, Benard N and Moreau E 2024 *Journal of Electrostatics* **130** 103950
[18] Chelih A, Bouadi M, Bouazza M, Yanallah K and Safa A 2024 *IEEE Transactions on Plasma Science* **52** 212
[19] Akishev Y S, Kochetov I V, Loboiko A I and Napartovich A P 2002 *Plasma Physics Reports* **28** 1049
[20] Napartovich A P, Akishev Y S, Deryugin A A, Kochetov I V, Pan'Kin M V and Trushkin N I 1997 *J. Phys. D: Appl. Phys.* **30** 2726
[21] Sattari P, Gallo C F, Castle G S P and Adamiak K 2011 *J. Phys. D: Appl. Phys.* **44** 155502
[22] Sattari P, Castle G S P and Adamiak K 2011 *IEEE Transactions on Industry Applications* **47** 1935

[23] Woo Seok K, Jin Myung P, Yongho K and Sang Hee H 2003 *IEEE Transactions on Plasma Science* **31** 504
[24] Kulikovsky A A 1997 *J. Phys. D: Appl. Phys.* **30** 441
[25] Tran T N, Golosnoy I O, Lewin P L and Georghiou G E 2011 *J. Phys. D: Appl. Phys.* **44** 015203
[26] Dordizadeh P, Adamiak K and Castle G S P 2016 *Journal of Electrostatics* **84** 73
[27] Dordizadeh P, Adamiak K and Peter Castle G S 2015 *J. Phys. D: Appl. Phys.* **48** 415203
[28] Dordizadeh P, Adamiak K and Castle G S P 2017 *Journal of Electrostatics* **88** 49
[29] Chen S, Li K and Nijdam S 2019 *Plasma Sources Science and Technology* **28** 055017
[30] Chen S, van den Berg R G W and Nijdam S 2018 *Plasma Sources Science and Technology* **27** 055021
[31] Ning W, Shang H, Li Y, Xiang W, Shen S, Huang X and Jia S 2025 *Plasma Sources Science and Technology* **34** 095001
[32] He H, Zhang W, Liu L, Luo B, Chen Y, Zhang S, Xiao M, Huang Y and Chen S 2024 *Plasma Sources Science and Technology* **33** 085008
[33] Yan H, Benard N and Moreau E 2023 *J. Appl. Phys.* **133** 013301
[34] Xiao M, Liu L, He H, Luo B, Che J and He J 2021 *J. Phys. D: Appl. Phys.* **55** 095203
[35] Ning W, Shen X, Yang S, Zhang Y, Huang X, Ren J and Jia S 2024 *Phys. Plasmas* **31** 083506
[36] Raizer Y P, Kisin V and Allen J 1991 *Gas Discharge Physics* (Berlin: Springer-Verlag)